Supporting Information for "Magnetic signature of vertically migrating aggregations in the ocean"

M. K. Fu [1]and J. O. Dabiri [1]

[1]Graduate Aerospace Laboratories and Department of Mechanical and Civil Engineering, California Institute of Technology, Pasadena, CA 91125

Contents of this file

1. Text S1 to S2
2. Figures S1 to S6

Additional Supporting Information (Files uploaded separately)

1. Captions for large Tables S1 to S2

Introduction Text S1 provides further details into the derivation of the electromagnetic field equations and results employed in the main manuscript. Text S2 provides additional details about the different velocity field models employed in the manuscript with additional notes on the computational aspects and results. Figures S1 - S6 provide clarification and illustration of the models and results discussed in Text S2. Tables S1 and S2 provide summaries of different velocimetry and magnetometry techniques, respectively.

Text S1.

Electromagnetic Theory

The electric current density, $\mathbf{j}$, induced by the motion of seawater can be determined from Ohm's Law given by

$$\mathbf{j} = \sigma \left(\mathbf{E} + \mathbf{u} \times \mathbf{B_{geo}} \right), \tag{1}$$

where σ is the electrical conductivity of the seawater (3-6 S/m), $\mathbf{E}$ is any applied or induced electric field, $\mathbf{u}$ is the fluid velocity field, and $\mathbf{B_{geo}}$ is the Earth's geomagnetic magnetic field (25,000-50,000 nT). The resulting electric current, $\mathbf{j}$, in turn, has an associated magnetic field perturbation, $\mathbf{b}$, which can be determined from the non-relativistic (magnetostatic) version of Ampere's Law as

$$\nabla \times \mathbf{b} = \mu_0 \, \mathbf{j}. \tag{2}$$

Here, μ_0 denotes the magnetic permeability of seawater ($\mu_0 = 4\pi \times 10^{-7}$ H/m), which is taken to be equal to the magnetic permeability of free space.

Substituting equation 2 into 1 for $\mathbf{j}$ gives the relation

$$\mathbf{E} = \frac{\nabla \times \mathbf{b}}{\mu_0 \, \sigma} - \mathbf{u} \times \mathbf{B_{geo}}. \tag{3}$$

If the temporal variations in the geomagnetic field are assumed to be small compared to temporal variations in the magnetic perturbation (i.e., $\partial B_{geo}/\partial t \ll \partial b/\partial t$), then the electric field in equation 3 can be related to the motionally-induced magnetic field, $\mathbf{b}$, through the Maxwell–Faraday Law of Induction:

$$\frac{\partial \mathbf{b}}{\partial t} = -\nabla \times \mathbf{E}. \tag{4}$$

Taking the curl of equation 3 allows equation 4 to be expressed as

$$\frac{\partial \mathbf{b}}{\partial t} = -\nabla \times \left(\frac{\nabla \times \mathbf{b}}{\mu_0 \, \sigma} - \mathbf{u} \times \mathbf{B_{geo}} \right). \tag{5}$$

The first and second terms on the right-hand side of equation 5 can be expanded and rewritten using the vector identities

$$\begin{aligned} -\nabla \times \left(\frac{\nabla \times \mathbf{b}}{\mu_0 \, \sigma} \right) = & \quad -\tfrac{\nabla \times (\nabla \times \mathbf{b})}{\mu_0 \, \sigma} - \nabla \left(\tfrac{1}{\mu_0 \sigma} \right) \times (\nabla \times \mathbf{b}) \\ = & \; -\tfrac{1}{\mu_0 \, \sigma} \left(\nabla \left(\nabla \cdot \mathbf{b} \right) - \nabla^2 \mathbf{b} \right) - \nabla \left(\tfrac{1}{\mu_0 \sigma} \right) \times (\nabla \times \mathbf{b}), \end{aligned} \tag{6}$$

and

$$\nabla \times (\mathbf{u} \times \mathbf{B_{geo}}) = \mathbf{u} \left(\nabla \cdot \mathbf{B_{geo}} \right) - \mathbf{B_{geo}} \left(\nabla \cdot \mathbf{u} \right) + \left(\mathbf{B_{geo}} \cdot \nabla \right) \mathbf{u} - \left(\mathbf{u} \cdot \nabla \right) \mathbf{B_{geo}}, \tag{7}$$

respectively. Using equations 6 and 7, equation 5 can be expressed as

$$\begin{aligned} \frac{\partial \mathbf{b}}{\partial t} = & -\frac{\left(\nabla \left(\nabla \cdot \mathbf{b} \right) - \nabla^2 \mathbf{b} \right)}{\mu_0 \, \sigma} - \nabla \left(\frac{1}{\mu_0 \sigma} \right) \times (\nabla \times \mathbf{b}) + \\ & \mathbf{u} \left(\nabla \cdot \mathbf{B_{geo}} \right) - \mathbf{B_{geo}} \left(\nabla \cdot \mathbf{u} \right) + \left(\mathbf{B_{geo}} \cdot \nabla \right) \mathbf{u} \; - \left(\mathbf{u} \cdot \nabla \right) \mathbf{B_{geo}}. \end{aligned} \tag{8}$$

Because the fluid flow is assumed to be incompressible, the velocity field will be solenoidal (i.e., divergence free), following:

$$\nabla \cdot \mathbf{u} = 0. \tag{9}$$

Similarly, by Gauss' Law of Magnetism, both magnetic fields are also solenoidal:

$$\nabla \cdot \mathbf{b} = 0 \quad ; \quad \nabla \cdot \mathbf{B_{geo}} = 0. \tag{10}$$

Using the constraints from equations 9 and 10, equation 8 reduces to

$$\frac{\partial \mathbf{b}}{\partial t} = \frac{1}{\mu_0\, \sigma}\nabla^2 \mathbf{b} - \nabla\left(\frac{1}{\mu_0 \sigma}\right) \times (\nabla \times \mathbf{b}) + (\mathbf{B_{geo}} \cdot \nabla)\, \mathbf{u} - (\mathbf{u} \cdot \nabla)\, \mathbf{B_{geo}}. \tag{11}$$

To further simplify the relation between seawater motion, $\mathbf{u}$, and the induced magnetic field perturbation, $\mathbf{b}$, additional information related to the flows of interest can be considered. The leading order dynamics of the magnetic field perturbation, $\mathbf{b}$, can be identified by substituting the variables in equation 11 for dimensionless variables that have been scaled by an appropriate, dimensional prefactor. These dimensionless variables are denoted with an $\sim$ overline and given by

$$\tilde{t} = t/T,$$

$$\tilde{\mathbf{b}} = \mathbf{b}/\beta,$$

$$\tilde{\mathbf{r}} = \mathbf{r}/L = [x, y, z]/L = [\tilde{x}, \tilde{y}, \tilde{z}],$$

$$\mathbf{u} = U\tilde{\mathbf{u}},$$

$$\sigma = \sigma_0 \tilde{\sigma}.$$

The magnitude of each prefactor (e.g., L, U, σ_0, and T) is determined by the flow configuration of interest. The corresponding magnetic field perturbation scale, β, remains to be determined. Substituting these variables into equation 11 gives

$$\left[\frac{\beta}{T}\right]\frac{\partial\tilde{\mathbf{b}}}{\partial\tilde{t}} = \left[\frac{\beta}{\mu_0\,\sigma_0 L^2}\right]\left(\tilde{\nabla}^2\tilde{\mathbf{b}} - \tilde{\nabla}\left(\frac{1}{\tilde{\sigma}}\right)\times\left(\tilde{\nabla}\times\tilde{\mathbf{b}}\right)\right) + \left[\frac{U\,|\mathbf{B_{geo}}|}{L}\right]\left(\hat{\mathbf{B}}_{\mathbf{geo}}\cdot\tilde{\nabla}\right)\,\tilde{\mathbf{u}} - \left[\frac{U\,\delta B_{geo}}{L}\right]\left(\tilde{\mathbf{u}}\cdot\tilde{\nabla}\right)\hat{\mathbf{B}}_{\mathbf{geo}}, \quad (12)$$

where $\hat{\mathbf{B}}_{\mathbf{geo}}$ is the unit vector aligned with the direction of the geomagnetic field and δB_{geo} is the scale of the variations in the geomagnetic field strength over the domain of interest. This choice of scaling takes a conservative approach where the gradients in the velocity, conductivity, and magnetic perturbation fields are assumed to scale the same as the scaling prefactor divided by the length scale, L. In this formulation, all the dimensionless variables are outside the brackets and are assumed to be on the order of unity if appropriately scaled. The prefactors contained within the brackets denote the scale of each term in the equation, quantifying their relative importance to the dynamics. Normalizing equation 12 by the scale $[U\ \ |\mathbf{B_{geo}}|\,L^{-1}]$ gives

$$\left[\frac{L\beta}{UT\,|\mathbf{B_{geo}}|}\right]\frac{\partial\tilde{\mathbf{b}}}{\partial\tilde{t}} = \left[\frac{\beta}{\mu_0\,\sigma_0 LU\,|\mathbf{B_{geo}}|}\right]\left(\tilde{\nabla}^2\tilde{\mathbf{b}} - \tilde{\nabla}\left(\frac{1}{\tilde{\sigma}}\right)\times\left(\tilde{\nabla}\times\tilde{\mathbf{b}}\right)\right) + \left(\hat{\mathbf{B}}_{\mathbf{geo}}\cdot\tilde{\nabla}\right)\tilde{\mathbf{u}} - \left[\frac{\delta B_{geo}}{|\mathbf{B_{geo}}|}\right]\left(\tilde{\mathbf{u}}\cdot\tilde{\nabla}\right)\,\hat{\mathbf{B}}_{\mathbf{geo}} \quad (13)$$

such that each of the prefactors is now a dimensionless quantity, and the scale of the $\left(\hat{\mathbf{B}}_{\mathbf{geo}}\cdot\tilde{\nabla}\right)\tilde{\mathbf{u}}$ term is normalized to unity. To identify which terms in equation 13 are of leading order, the relative magnitudes of the terms involving the magnetic field perturbation, $\mathbf{b}$, can be compared. The ratio between the prefactors of the unsteadiness term on the left-hand side and the Laplacian and conductivity gradient terms on the right-hand side is given by

$$\left[\frac{L\beta}{UT\,|\mathbf{B_{geo}}|}\right]\Big/\left[\frac{\beta}{\mu_0\,\sigma_0 LU\,|\mathbf{B_{geo}}|}\right]=\left[\frac{L^2\mu_0\,\sigma_0}{T}\right].$$

Assigning representative values for the scaling parameters based on the relevant oceanic context of $\sigma_0 = 6$ S/m, $\mu_0 = 4\pi \times 10^{-7}$ H/m, $L = 1000$ m, and $T = 1$ hr, yields $L^2\mu_0\sigma_0 T^{-1} = \mathcal{O}(10^{-3})$. The value of this ratio indicates that contributions from the unsteadiness term to the dynamics of equation 13 are approximately three orders of magnitude smaller than those of the Laplacian and conductivity gradient terms and can likely be neglected. In this case, it can also be concluded that the scaling prefactor of the Laplacian term in equation 13, $[\beta(\mu_0\,\sigma_0 LU\,|\mathbf{B_{geo}}|)^{-1}]$, must be of leading order to ensure that the magnetic perturbation, $\mathbf{b}$, is still included in the leading order dynamics.

Finally, it remains to be established if the final term in equation 13, which scales as $\left[\delta B_{geo}\,|\mathbf{B_{geo}}|^{-1}\right]$, is of leading order. The geomagnetic field strength, $|\mathbf{B_{geo}}|$, is found to vary less than 0.1% over domain sizes of L =1000 m (Chulliat et al., 2020) indicating that $\left[\delta B_{geo}\,|\mathbf{B_{geo}}|^{-1}\right] = \mathcal{O}(10^{-3})$. This similarly small ratio indicates that contributions from the last term are also not of leading order for the flows of present interest and can similarly be neglected. Having now assessed the scale of each prefactor, the leading order dynamics in equation 13 are found to be order unity, and it can be concluded that $[\beta^{-1}\mu_0\,\sigma_0 LU\,|\mathbf{B_{geo}}|] = \mathcal{O}(1)$ to ensure it is retained in the leading order dynamics. Following the above scaling analysis, the leading order terms from equation 13 that relate the seawater motion, $\mathbf{u}$, to the induced magnetic field perturbation, $\mathbf{b}$, are given by:

$$0 = \tilde{\nabla}^2\tilde{\mathbf{b}} - \tilde{\nabla}\left(\frac{1}{\tilde{\sigma}}\right)\times\left(\tilde{\nabla}\times\tilde{\mathbf{b}}\right) + \left(\hat{\mathbf{B}}_{\mathbf{geo}}\cdot\tilde{\nabla}\right)\tilde{\mathbf{u}}, \tag{14}$$

or in dimensional terms,

$$0 = \frac{1}{\mu_0\,\sigma}\nabla^2\mathbf{b} + (\mathbf{B_{geo}}\cdot\nabla)\,\mathbf{u} - \nabla\left(\frac{1}{\mu_0\sigma}\right)\times(\nabla\times\mathbf{b})\,. \tag{15}$$

In cases where the electrical conductivity of the seawater is assumed to be horizontally homogeneous (i.e., $\sigma = \sigma(z)$), further simplification of equation 15 can be observed when expressed in component wise form as:

$$\left(\frac{\partial^2 b_x}{\partial x^2} + \frac{\partial^2 b_x}{\partial y^2} + \frac{\partial^2 b_x}{\partial z^2}\right) = -\mu_0\sigma(z)\left(B_x\frac{\partial u}{\partial x} + B_y\frac{\partial u}{\partial y} + B_z\frac{\partial u}{\partial z}\right) + \frac{1}{\sigma(z)}\frac{\partial\sigma(z)}{\partial z}\left(\frac{\partial b_z}{\partial x} - \frac{\partial b_x}{\partial z}\right) \tag{16a}$$

$$\left(\frac{\partial^2 b_y}{\partial x^2} + \frac{\partial^2 b_y}{\partial y^2} + \frac{\partial^2 b_y}{\partial z^2}\right) = -\mu_0\sigma(z)\left(B_x\frac{\partial v}{\partial x} + B_y\frac{\partial v}{\partial y} + B_z\frac{\partial v}{\partial z}\right) + \frac{1}{\sigma(z)}\frac{\partial\sigma(z)}{\partial z}\left(\frac{\partial b_z}{\partial y} - \frac{\partial b_y}{\partial z}\right) \tag{16b}$$

$$\left(\frac{\partial^2 b_z}{\partial x^2} + \frac{\partial^2 b_z}{\partial y^2} + \frac{\partial^2 b_z}{\partial z^2}\right) = -\mu_0\sigma(z)\left(B_x\frac{\partial w}{\partial x} + B_y\frac{\partial w}{\partial y} + B_z\frac{\partial w}{\partial z}\right) \tag{16c}$$

where $B_{geo} = [B_x,\, B_y,\, B_z]$. While the horizontal components of the magnetic perturbation, b_x and b_y, each depend on the vertical gradient of electrical conductivity (see equations 16a and 16b), the equation for b_z (equation 16c) no longer has such dependencies when $\sigma = \sigma(z)$. Furthermore, because equation 16c has no dependency on b_x or b_y, it is a 3D Poisson equation for b_z and can be solved using the free space Green's function as

$$b_z(\mathbf{r}) = \iiint_V \frac{-\mu_0\sigma(z)}{4\pi\,|\mathbf{r}-\mathbf{r}'|}\left(B_x\frac{\partial w}{\partial x'} + B_y\frac{\partial w}{\partial y'} + B_z\frac{\partial w}{\partial z'}\right)\mathrm{d}^3r' \tag{17}$$

where the local conductivity field is included in the forcing term of the integrated function. The same is not true, however, for the horizontal components which depend on horizontal gradients in b_z. This complication requires alternative approaches such as determining the

vertical component of the magnetic field, b_z, and then iteratively solving for the horizontal components or solving the entire set of equations numerically through a relaxation method.

In cases when σ is constant over the entire domain, then equation 15 simplifies instead to

$$0 = \frac{1}{\mu_0\,\sigma}\nabla^2\mathbf{b} + (\mathbf{B_{geo}}\cdot\nabla)\,\mathbf{u} \tag{18}$$

which is a vectorized Poisson equation in 3D. Here, each component can be solved with the free space Green's function for the 3D Poisson equation through the integral relation

$$\mathbf{b}(\mathbf{r}) = \iiint_V \frac{-\mu_0\sigma\ \,(\mathbf{B_{geo}}(\mathbf{r}')\cdot\nabla)\,\mathbf{u}(\mathbf{r}')}{4\pi\,|\mathbf{r}-\mathbf{r}'|}\,\mathrm{d}^3r'. \tag{19}$$

Expressing each vector component of equation 19 with $B_{geo} = [B_x,\, B_y,\, B_z]$ gives

$$b_x(\mathbf{r}) = \iiint_V \frac{-\mu_0\sigma}{4\pi\,|\mathbf{r}-\mathbf{r}'|}\left(B_x\frac{\partial u}{\partial x'} + B_y\frac{\partial u}{\partial y'} + B_z\frac{\partial u}{\partial z'}\right)\mathrm{d}^3r' \tag{20a}$$

$$b_y(\mathbf{r}) = \iiint_V \frac{-\mu_0\sigma}{4\pi\,|\mathbf{r}-\mathbf{r}'|}\left(B_x\frac{\partial v}{\partial x'} + B_y\frac{\partial v}{\partial y'} + B_z\frac{\partial v}{\partial z'}\right)\mathrm{d}^3r' \tag{20b}$$

$$b_z(\mathbf{r}) = \iiint_V \frac{-\mu_0\sigma}{4\pi\,|\mathbf{r}-\mathbf{r}'|}\left(B_x\frac{\partial w}{\partial x'} + B_y\frac{\partial w}{\partial y'} + B_z\frac{\partial w}{\partial z'}\right)\mathrm{d}^3r' \tag{20c}$$

where $\mathbf{r} = (x, y, z)$ and $\mathbf{r}' = (x', y', z')$. The above relations are valid inside the ocean and the Earth's surface. Above the ocean, where there is no electrical current or conductivity, the fields are determined by Laplace's equation for the scalar potential $\nabla V = -\mathbf{b}$ such that $\nabla^2 V = -\nabla\cdot\mathbf{b} = 0$.

Text S2.

Velocity Field Models

Having established the relationship between the seawater motion, $\mathbf{u}$, and the induced magnetic field perturbation, $\mathbf{b}$, the magnetohydrodynamic signature of vertically migrating aggregations can be derived for representative velocity fields. In the following section, three different models for the biologically generated velocity field will be considered. First, the flow induced from vertically migrating aggregations is modeled using a Dirac delta distribution in the xy-plane (i.e., horizontal plane) having a strength, Q, representing the volumetric flow rate caused by the aggregation wake. This configuration mimics the scenario in which the induced flow is confined to a narrow radial extent in the horizontal plane relative to the size of the domain and assumes a homogeneous velocity signature along the vertical extent of the domain.

The next model considers the induced flow to have a Gaussian distribution in the horizontal plane with a characteristic finite width, ς_0, with centerline vertical velocity, W, along the vertical axis. Similar to the previous model, the velocity signature is assumed to extend uniformly along the vertical extent of the domain.

In the final model, the effect of the aggregation is modelled using an actuator disk (Rankine, 1865) with a steady rate of vertical climb. In this case, the velocity field due to the migration is no longer homogeneous in the vertical direction. Instead, the velocity signature is modeled as linearly expanding wake with a Gaussian velocity profile that extends downstream from the aggregation position and has a negligible influence upstream.

When subjected to a horizontal geomagnetic field such as that present near the equator, each of these velocity field models generates a magnetic signature, $\mathbf{b}$, that is poloidal, i.e.,

having primarily a vertical component. The magnitude of the vertical component is found to decay inversely with distance from the induced flow and be modulated sinusoidally around the vertical axis of the migration direction. Importantly, the slower decay of the magnetic signature (i.e., $b \sim r^{-1}$) compared to the velocity signature (i.e., $w \sim e^{-r}$) indicates that the physical signature of a vertical migration of swimming plankton is potentially detectable with modern magnetometry techniques from distances where the induced flow cannot be detected. The magnetic field could provide additional insight into the bulk fluid transport associated with biologically induced flow, as well as the flow induced by other vertical transport processes in the ocean.

Dirac Delta Migration Model

The biologically generated velocity field stemming from the vertically migrating aggregations, $\mathbf{u}(\mathbf{r})$, is modelled first with a Dirac delta distribution in the horizontal plane given by:

$$\mathbf{u}(\mathbf{r}) = [u,\, v,\, w] = [0,\, 0,\, \pm Q\delta(x)\delta(y)]\,, \tag{21}$$

where $\pm Q$ is the volumetric flow rate associated with the induced flow, respectively. This velocity distribution is most representative when the characteristic width of the aggregation is small compared to the vertical extent of the velocity signature and the distances at which the magnetic signature is being measured. Similar to the previous section, the magnetic field signature can be related to the specific flow parameters through dimensional analysis. In this model, there are eight physical parameters: the magnitude of the magnetic signature, b, the geomagnetic field strength, B_{geo}, volumetric flow rate, Q, electrical conductivity of the fluid, σ, magnetic permeability of seawater, μ_0, fluid

density, ρ, kinematic viscosity, ν, and distance from the migration, ϱ, along with four associated dimensions: mass, length, time, and electric current. Through the applications of the Buckingham-π theorem, four dimensionless groups can be identified such that the functional dependence of b can be expressed as

$$\frac{b}{B_{geo}} \cdot = f_1\left(N, \mathrm{R}_\varrho, m\right) \tag{22}$$

where $N \equiv B_{geo}^2 \varrho^3 \sigma/(\rho Q)$ is the Stuart Number, $\mathrm{R_m} \equiv Q\varrho^{-1}\sigma\mu_0$ is the dimensionless distance from the aggregation, and $m \equiv \nu \cdot \sigma \cdot \mu_0$ is the magnetic viscosity ratio. For parameter values representative of the flow of present interest, (i.e., $B_{geo} = 25\mu$T, $Q = 40\,\mathrm{m}^3$/s m, $\sigma = 6$ S/m, $\rho = 1.025$ g/mL, $U = 5$ mm/s, and $\varrho = 1000$m), the Stuart Number is $N = O(10^{-5})$, indicating that electromagnetic forces within the fluid are much smaller than inertial forces, consistent with the assumptions of our model. Similarly, the dimensionless magnetic signature $b \cdot B_{geo}^{-1}$ is expected to exhibit a functional dependence on the dimensionless distance, $\mathrm{R_m} \equiv Q\varrho^{-1}\sigma\mu_0$, which has the form of a magnetic Reynolds number.

To specify the functional form of the magnetic signature, $\mathbf{b}$, the model velocity field can be analyzed using the Green's function approach described in Text S1 with a known geomagnetic field, $\mathbf{B_{geo}}$. Here, the geomagnetic field is taken to be constant over the domain without declination (B_x) and inclination (B_z) such that

$$\mathbf{B}(\mathbf{r}) = [0, B_y, 0] \tag{23}$$

where B_x is prescribed to be aligned with the East-West direction, B_y is aligned with the geographic North-South direction and B_z is aligned with the vertical. This choice of geo-

magnetic field is representative of equatorial regions, where biologically generated mixing has been proposed as a potential contributor to the Meridional Overturning Circulation (MOC). (Munk, 1966; Dewar et al., 2006; Dabiri, 2010). It also follows from equations 20c - 20c that the homogeneity of the vertical velocity field along the vertical (z) direction restricts the dependence of the vertical component of the magnetic signature, b_z, to only horizontal components of the geomagnetic field (i.e., B_x and B_y).

Substituting equations 21 and 23 into equations 20a-20c gives

$$\mathbf{b}(\mathbf{r}) = [b_x,\ b_y,\ b_z] = \left[0,\ 0,\ \iiint_V \frac{B_y\ \mu_0\ \sigma\ Q\delta(x')\frac{\mathrm{d}\delta(y')}{\mathrm{d}y'}}{4\pi\sqrt{(x-x')^2+(y-y')^2+(z-z')^2}}\,\mathrm{d}x'\mathrm{d}y'\mathrm{d}z'\right]. \tag{24}$$

Using the identity

$$\int f(x)\delta'(x)\mathrm{d}x = \int -f'(x)\delta(x)\mathrm{d}x, \tag{25}$$

integration in the x and y directions yields

$$\begin{aligned}
b_z &= B_y\ \mu_0\ \sigma\ Q \iiint_V \frac{1}{4\pi\sqrt{x^2+(y-y')^2+(z-z')^2}}\,\frac{\mathrm{d}\delta(y')}{\mathrm{d}y'}\mathrm{d}x'\mathrm{d}y'\mathrm{d}z' \\
b_z &= B_y\ \mu_0\ \sigma\ Q \iint \frac{(y-y')}{4\pi\left(x^2+(y-y')^2+(z-z')^2\right)^{3/2}}\,\delta(y')\mathrm{d}y'\mathrm{d}z' \\
b_z &= B_y\ \mu_0\ \sigma\ Q \int \frac{y}{4\pi\left(x^2+y^2+(z-z')^2\right)^{3/2}}\,\mathrm{d}z'. \\
b_z &= B_y\ \mu_0\ \sigma\ Q \frac{y\ H}{2\pi\left(x^2+y^2\right)\sqrt{H^2+x^2+y^2}}
\end{aligned}$$

for constant σ. In scenarios when σ varies along the z direction, it should remain in the integrand. Finally, integrating in the z-direction from $-H$ to H, where $2H$ is the height

of the velocity signature, yields

$$b_z = B_y\ \mu_0\ \sigma\ Q \frac{y\ H}{2\pi\ (x^2+y^2)\ \sqrt{H^2+x^2+y^2}}.$$

In the limit of $H \to \infty$, the relation for the magnetic field signature given by

$$\frac{b_z}{B_y} = \frac{y\ \mu_0\ \sigma\ Q}{2\pi\ (x^2+y^2)} = \frac{1}{2\pi}\frac{\mu_0\ \sigma\ Q\ \sin\theta}{\sqrt{x^2+y^2}}. \tag{26}$$

This resulting expression is consistent with the above dimensional analysis, revealing that the strength of the magnetic field perturbation decays inversely with distance from the velocity signature and is modulated sinusoidally by the azimuthal angle, θ, from the positive x-axis.

Gaussian Jet Model

The second model for $\mathbf{u}(\mathbf{r})$ is given by a unidirectional flow along the z direction with Gaussian distribution along the x and y directions. For distributions centered on the domain origin, the velocity field for induced flow can be expressed as

$$\mathbf{u}(\mathbf{r}') = [u,\ v,\ w] = \left[0,\ 0,\ \pm W \exp\left(\frac{-\left(x'^2+y'^2\right)}{2\varsigma_0^2}\right)\right] \tag{27}$$

where W is the velocity scale of the induced flow and ς_0 is the characteristic width of the jet. A contour map of the vertical velocity distribution for downwelling is shown over the xy-plane in figure S1(a). Integrating equation 27 over the xy-plane reveals that the net volumetric flow rate associated with this induced flow model is $Q = \pm 2\pi\, W\, \varsigma_0^2$. Taking the limit of $\varsigma_0 \to 0$ and $W \to \infty$ where the volume flux, Q, is finite, i.e., $Q = 2\pi\varsigma_0^2 W =$ constant, recovers the Dirac delta distribution from Text S1 given by equation 21.

Similar to the previous model, the Earth's magnetic field is taken as constant with a negligible declination (B_x) and inclination (B_z) and B_y aligned with the North-South direction.

With the velocity fields (equation 27) and applied magnetic fields (equation 23) known, equations 20a-20c can be simplified as

$$\mathbf{b}(\mathbf{r}) = [b_x,\, b_y,\, b_z] \,=\, \left[0,\; 0,\; \mu_0\,\sigma \iiint_V \frac{1}{4\pi\,|\mathbf{r}-\mathbf{r}'|}\,\left(B_y \frac{\partial w}{\partial y'}\right) \mathrm{d}^3 r'\right] \tag{28}$$

where

$$\frac{\partial w}{\partial y'} = y' \frac{W}{\varsigma_0^2} \exp\left(\frac{-\left(x'^2 + y'^2\right)}{2\varsigma_0^2}\right). \tag{29}$$

Expanding the b_z component gives

$$b_z = \,\mu_0\,\sigma \iiint_V \frac{B_y}{4\pi\,|\mathbf{r}-\mathbf{r}'|}\,\left(y' \frac{W}{\varsigma_0^2} \exp\left(\frac{-\left(x'^2 + y'^2\right)}{2\varsigma_0^2}\right)\right) \mathrm{d}^3 r'. \tag{30}$$

Rescaling the equation with length scale, ς_0, gives a pre-factor of ς_0^3 and new dimensionless variables of integration: $\tilde{\mathbf{r}} = \mathbf{r}/\varsigma_0$, $\tilde{x}' = x'/\varsigma_0$, $\tilde{y}' = y'/\varsigma_0$, and $\tilde{z}' = z'/\varsigma_0$:

$$\tilde{b}_z(\tilde{\mathbf{r}}) = \frac{b_z(\tilde{\mathbf{r}})}{\mu_0\,\sigma\,B_y\,W\,\varsigma_0} = \frac{1}{4\pi} \iiint \frac{\tilde{y}'}{|\tilde{\mathbf{r}}-\tilde{\mathbf{r}}'|} \exp\left(\frac{-\left(\tilde{x}'^2 + \tilde{y}'^2\right)}{2}\right) \mathrm{d}\tilde{x}'\,\mathrm{d}\tilde{y}'\,\mathrm{d}\tilde{z}', \tag{31}$$

which can be solved numerically.

Numerical Approach and Results

To compute the integral in equation 31, the velocity field is discretized onto a 3D domain ranging from $-5\varsigma_0$ to $5\varsigma_0$ in each of the x and y directions and from $-320\varsigma_0$ to $320\varsigma_0$ in the vertical (i.e., z-direction) using $[N_x,\, N_y,\, N_z] = [64,\, 64,\, 2560]$ gridpoints to mimic a long vertical extent of downwelling. The magnetic field was evaluated on a larger domain on the xy-plane (i.e., $z = 0$) at 50 logarithmically spaced locations ranging

from $x, y = 0.01 - 1000$. A grid convergence study of the velocity field discretization was conducted to verify that the root-mean-square differences for the different resolutions were less than 1% of the global root-mean-square variations. Further, a domain study using different heights from $H = 80\varsigma_0 - 640\varsigma_0$ was conducted to observe their effects on the power law behavior ranges. All computations were performed on an Nvidia RTX Quadro 5000 GPU.

The numerical results for the dimensionless vertical magnetic field $\tilde{b}_z$ on the xy-plane are shown in figure S1(b). Compared to the Gaussian velocity signature shown in figure S1(a), the magnetic signature persists much further away from the location of induced flow and exhibits a lobed structure. More precisely, the variation of the magnetic signature with azimuthal angle follows a sinusoidal dependence within the xy-plane and is shown in figure S2(a) as a function of azimuthal locations where $\varrho \equiv \sqrt{x^2 + y^2} = \varsigma_0$, consistent with the simpler Dirac delta model.

The variation of the magnetic signature with distance is found to exhibit three distinct scaling regimes, which are shown in figure S2(b) at locations along the y-axis. The first regime occurs within the vicinity of the velocity signature ($y/\varsigma_0 \ll 1$). Here, the strength of the magnetic signature is largest due to the proximity to the finite velocity gradients and grows with distances away from the migration axis. The second regime begins outside the velocity signature region ($y/\varsigma_0 > 1$) and extends to $y/\varsigma_0 \approx H/\varsigma_0$. Here, the signal begins to decay inversely with distance from the migration (i.e., $(y/\varsigma_0)^{-1}$) and most closely emulates the behavior and assumptions of the Dirac delta model. The final regime is encountered at distances comparable to the height of the migration. There, the signal

begins to exhibit a stronger decay, scaling nominally the inverse square of distance from the migration (i.e.,$(y/\varsigma_0)^{-2}$), and is dominated by the effects of the finite domain size.

The collection of these distinct behaviors in the magnetic signature are qualitatively analogous to the Rankine model of a vortex in viscous flow. In that model, the azimuthal velocity magnitude is found to increase linearly within a viscously dominated core and decay inversely with distances outside of the core. Here, an analogous behavior is observed in the magnetic signature, albeit with an additional sinusoidal modulation along the azimuth. The analogous Rankine model for the magnetic signature is given by the piecewise equation:

$$\tilde{b}_z(\tilde{\mathbf{r}}) = \begin{cases} y/(2\varsigma_0) & \varrho/\varsigma_0 \leq \sqrt{2} \\ \varsigma_0 y/\varrho^2 & \sqrt{2} \leq \varrho/\varsigma_0 \leq H/(\varsigma_0) \\ H\varsigma_0 y/\varrho^3 & \varrho/\varsigma_0 > H/(\varsigma_0) \end{cases} \tag{32}$$

where $\varrho = \sqrt{x^2 + y^2}$.

To determine the measurement sensitivity required to detect the magnetic signature, representative values for each parameter are chosen as $B_{geo} = 25\mu$T, $\varsigma_0 = 100$ m, $\sigma = 5$ S/m, $W = 1$ cm/s, and substituted for the dimensionless variables. The nominal scale of the vertical magnetic signature is found to be $\mu_0 \sigma B_y W \varsigma_0 = 157$ pT. Recasting the data from figure S2(b) in terms of these dimensional parameters gives the distributions shown in figure S3 for both the vertical magnetic and velocity components as a function of distance from the aggregation center. Superimposed on each distribution are the resolution or sensitivity limit for select measurement techniques for each parameter. A detailed tabulation of velocimetry and magnetometry techniques is compiled in Tables S1 and S2, respectively. For the velocity field, common techniques such as Acoustic

Doppler Current Profilers (ACDPs) (Nortek, 2021c, 2021a; Park & Hwang, 2021), Acoustic Doppler Velocimeters (Nortek, 2021b; Teledyne RD Instruments, 2009b; Cisewski et al., 2010; Teledyne RD Instruments, 2009a; Cisewski et al., 2021), and Particle Image Velocimetry (PIV) (Bertuccioli et al., 1999; Katija & Dabiri, 2008; Wang et al., 2012; Jin, 2019), all have resolution limits close to a few millimeters per second. Consequently, these techniques are suitable for observing upwelling and downwelling currents from migrating aggregates of zooplankton, which are typically on the order of a few centimeters per second (Wilhelmus & Dabiri, 2014; Houghton et al., 2018; Cisewski et al., 2010, 2021; Omand et al., 2021). However, as can be seen in figure S3, the Gaussian decay of the velocity signature confines the usefulness of these techniques to the immediate vicinity of the velocity signature, with each technique reaching its sensitivity floor within a distance of $2\varsigma_0 - 3\varsigma_0$ of the aggregation center. Quantifying the bulk fluid transport due to the migration with these velocimetry techniques is conceptually straightforward and involves measuring the vertical velocity distribution within the aggregation core and spatially integrating the results.

Even though the resolvable velocity signature is confined to a range comparable to the aggregation width, ς_0, the magnetic signature is potentially detectable at ranges at least an order of magnitude larger. This feature is enabled both by the persistence of the magnetic signature due to the inherent nonlocality of the magnetic field and the advancements in the capability of modern magnetometry techniques. For example, commercial fluxgate magnetometers (Bartington Instruments, 2022; Magson GmbH, 2022; Metrolab Technology SA, 2022) and emerging quantum sensing techniques such as Nitrogen-vacancy (NV)

centers (Wolf et al., 2015) have sensitivities on the order of $1 - 10\,\mathrm{pT}/\sqrt{\mathrm{Hz}}$, which are theoretically detect this magnetic signature up to $100\varsigma_0$ away along the N-S axis.

A potential benefit of this feature is the ability to locate instance of biogenic mixing via their magnetic signature. As seen in figure S3, in order to locate an instance of biogenic upwelling and downwelling via one of the localized velocimetry techniques (e.g., ADV), one would effectively need to be collocated with the aggregation wake. This limitation is not as applicable to ADCPs, which are capable of measuring linear velocity profiles at-a-distance. However, it is still necessary for the interrogation volume to intersect with the aggregation velocity wake in order to detect the biogenic flow. In contrast, the magnetic signature is inherently a nonlocal quantity that extends far beyond that of the velocity wake. While the inherent scale of the biogenic magnetic signature is small compared to the Earth's geomagnetic field, such a signal is potentially detectable with existing magnetometry techniques, including commercially available fluxgate magnetometer. Determining the size of the magnetic signature and mapping its distribution can potentially be accomplished with even a handful of magnetometers while also helping to identify the location of the aggregation and its velocity signature.

Low Aspect Ratio Aggregations - Actuator Disk Model

Induced velocity due to vertically migrating aggregations

In contrast to the previous models, where the velocity signature was assumed to have a long extent in the vertical direction, the current model considers the case where the vertical extent of the aggregation, H, is not only finite but much smaller than its characteristic width of the aggregation, D. In this low aspect ratio configuration, the aggregation can

be modeled as an actuator disk (Rankine, 1865; Houghton, 2019) in a steady rate of vertical climb. The velocity signature due to the migration is no longer homogeneous in the vertical direction but is instead confined to the region downstream of the aggregation location. In this section, the velocity induced by the vertical migration is related to the properties of the animals that comprise the aggregation following Houghton (2019). This induced velocity is then synthesized with the linearly expanding jet model based on actuator disk theory.

One approach to estimate the induced velocity due to the migration is the analysis proposed by Houghton (2019), which is reproduced below. In this approach, illustrated in figure S4, the vertically migrating aggregation is modeled as an actuator disk with diameter, D, that is in a steady upward climb (i.e., no acceleration) of velocity, W_v. By conservation of momentum, the thrust force from the vertical swimming (F_T) is balanced by the slight negative buoyancy of the aggregation (F_B) and the fluid drag on the swimmers (F_D). This force balance can be expressed

$$|F_T| = F_B + F_D = N\left[\Delta\rho\frac{4\pi a_r}{3}\left(\frac{d}{2}\right)^3\right] + N\left[\frac{\rho}{2}C_D W_v^2\pi\left(\frac{d}{2}\right)^2\right] \tag{33}$$

where, N is the number of animals, d is the body width of the animal, $a_r = \ell/d$ is the animal body length-to-width ratio, $\Delta\rho$ is the difference in density between the animal and the seawater. To simplify the analysis, the volume of the animal is approximated using the volume of a prolate spheroid.

The thrust force generated by the climbing aggregation can be related to the induced velocity experienced by the aggregation, Δw_0, through the relationship

$$F_T = \frac{1}{2}\rho\pi D^2 \Delta w_0 \left(W_v + \Delta w_0\right). \tag{34}$$

The above equation indicates that the thrust force experienced by the migrating aggregation is balanced by the downward momentum injected into the fluid by the swimmers. In the far field, the pressure recovery allows the thrust force from the aggregation to be related to the jet velocity, W_w, through

$$F_T = \frac{1}{2}\rho A_D W_w^2 = \frac{\pi}{8}\rho\pi D^2 W_w^2. \tag{35}$$

Using equations 34 and 33, the induced velocity of the aggregation in climb can be solved for as

$$\Delta w_0 = \sqrt{\frac{W_v^2}{4} + \frac{(F_B + F_D)}{2\rho A_D}} - \frac{W_v}{2} \tag{36}$$

If the disk is in a steady climb where the thrust is balanced by the weight of the aggregation and the drag on the disk, then the induced velocity term, $\frac{(F_B+F_D)}{2\rho A_D}$, can be expressed as

$$\frac{(F_B + F_D)}{2\rho A_D} = \frac{2N}{\rho\pi D^2}\left(\frac{\Delta\rho g 4\pi a_r}{3}\left(\frac{d}{2}\right)^3 + \frac{\rho}{2}C_D W_v^2 \pi \left(\frac{d}{2}\right)^2\right)$$
$$\frac{(F_B + F_D)}{2\rho A_D} = \frac{d^2}{4}\frac{N}{D^2}\left(\frac{4a_r}{3}\frac{\Delta\rho}{\rho}gd + C_D W_v^2\right)$$

Substituting the animal number density $\Phi = 4N/(\pi H D^2)$ gives

$$\frac{(F_B + F_D)}{2\rho A_D} = \Phi\frac{\pi H d^2}{16}\left(\frac{4a_r}{3}\frac{\Delta\rho}{\rho}gd + C_D W_v^2\right). \tag{37}$$

Substituting equation 37 into equation 36 gives

$$\Delta w_0 = \sqrt{\frac{W_v^2}{4} + \Phi \frac{\pi H d^2}{16} \left(\frac{4 a_r}{3} \frac{\Delta \rho}{\rho} g d + C_D W_v^2 \right)} - \frac{W_v}{2} \tag{38}$$

In circumstances where the induced velocity of the migrating aggregation is not known or cannot be measured, equation 38 can be employed with quantities based solely on the aggregation properties and rate of climb.

Linearly expanding jet model

While the vertical velocity profile is still assumed to have a Gaussian distribution in the horizontal plane, the width of the jet is prescribed to expand linearly with the distance downstream of the aggregation following Bastankhah and Porté-Agel (2014, 2016) and Shapiro et al. (2018). In the inertial frame of the migrating aggregation climbing with an upward velocity, W_v, the surrounding vertical velocity field is given by:

$$w(x, y, z) = -W_v - \Delta w(z) \frac{D^2}{8 \varsigma_0^2} \exp \left(\frac{-(x^2 + y^2)}{2 \varsigma_0^2 d_w(z)^2} \right). \tag{39}$$

Here the aggregation is centered on the domain origin, $\Delta w(z)$ is the vertical velocity deficit along the jet centerline, ς_0 is the characteristic width of the jet at the streamwise location of the aggregation taken to be $\varsigma_0 = 0.235D$ (Shapiro et al., 2018), and $d_w(z)$ is the dimensionless spreading function of the jet as a function of distance downstream of the aggregation. The jet spreading function is modeled as a linear expansion similar to the Jensen wake model (Jensen, 1983) and is given by the function

$$d_w(z) = 1 + k_w \ln \left(1 + \exp \left(\frac{2(z-1)}{D} \right) \right) \tag{40}$$

from Shapiro et al. (2018) with jet expansion coefficient, $k_w \approx 0.0834$. The corresponding centerline velocity deficit for the aggregation jet is given by

$$\Delta w(z) = \frac{\Delta w_0}{d_w^2(z)} \frac{1}{2} \left[1 + \text{erf}\left(\frac{z\sqrt{2}}{D} \right) \right] \tag{41}$$

where Δw_0 denotes the induced velocity at the center of the aggregation and is associated with the thrust force from to the vertically migrating aggregation. This parameter is also assumed to depend on the properties of the aggregation and will be discussed in the following section.

A mean entertainment velocity, u_ϱ, due to the vertical velocity field, w, can be modeled for an axisymmetric mean flow field using the incompressibility condition. The continuity equation for incompressible flow in cylindrical coordinates is given by

$$\nabla \cdot \mathbf{u} \implies \frac{1}{\varrho} \frac{\partial(\varrho u_\varrho)}{\partial \varrho} + \frac{\partial w}{\partial z} = -\frac{1}{\varrho} \frac{\partial u_\phi}{\partial \phi} = 0. \tag{42}$$

where z is the vertical coordinate, ϕ be the azimuthal angle, and ϱ be the radial coordinate in the horizontal. Assuming the mean velocity field to be axisymmetric lets the azimuthal velocity component, u_ϕ be zero and simplifies equation 42 to be

$$\frac{1}{\varrho} \frac{\partial(\varrho u_\varrho)}{\partial \varrho} = -\frac{\partial w}{\partial z}.$$

Solving for the radial velocity gives

$$u_\varrho(z, \varrho) = -\frac{1}{\varrho} \int_0^\varrho \varrho' \frac{\partial w}{\partial z}(z, \varrho') d\varrho'. \tag{43}$$

Combining equations 39, 41, 40, and 43 gives an axisymmetric mean velocity field associated with the vertical migration of a low aspect ratio aggregation. This velocity field

can be inserted into equations 20a-20c using the following transformation into Cartesian velocities:

$$u(z, \varrho, \theta) = u_\varrho \cos(\theta)$$

$$v(z, \varrho, \theta) = u_\varrho \sin(\theta)$$

$$w(z, \varrho, \theta) = w$$

Numerical Approach and Results

Similar to the previous section, the Green's function of the jet velocity was numerically integrated over the 3D domain ranging from $-10D$ to $10D$ in each of the x and y directions and from $-400D$ to $400D$ in the vertical (i.e., z-direction) using $[N_x, N_y, N_z] = [88, 88, 3520]$ grid points. The magnetic field was evaluated on a larger domain on the yz-plane (i.e., $x = 0$) at 100 logarithmically spaced locations ranging from $x, y = 0.01 - 1000$. As before, the Earth's magnetic field is taken to be both constant over the velocity field with a negligible declination and inclination such that only B_y is nonzero. In contrast to the previous velocity models, the semi-infinite extent of the velocity signature in the vertical (z) direction requires that the magnetic signature now have horizontal components to ensure that the magnetic field lines are closed. These horizontal components, however, are much smaller than the vertical component due the entrainment velocity and its horizontal gradients being much smaller than those of the vertical velocity component (i.e., jet velocity).

Unlike the previous velocity models, which feature vertical homogeneity in the velocity field, the actuator disk model assumes a minimal velocity signature far upstream of the aggregation and an expanding jet downstream of the migration. The resulting jet velocity given by equations 39 - 41 is shown in figure S5(a) as a contour map in the yz-plane with the nominal jet spreading of $2\varsigma d_w(z)$ (see equation 40) shown as a dashed line. The vertical component of the associated magnetic signature is shown in figure S5(b) as a contour map in the yz-plane against the same jet spreading function. Despite the reduced vertical extent of the jet, the magnetic signature is still observed to persist at horizontal distances much larger than the jet width for all values of z downstream of the aggregation.

Substituting representative parameters $B_{geo} = 25\mu$T, $D = 100$ m, $\sigma = 5$ S/m, and $\Delta w_0 = 1$ cm/s into these distributions again gives a magnetic signature scale of $\mu_0\sigma\Delta w_0 B_y D = 157$ pT. Select profiles of the vertical magnetic and velocity components are shown along the y-axis in figure S6 with the respective resolution/sensitivity limits of different measurement techniques. Similar to the previous analysis, common techniques such as Acoustic Doppler Current Profilers (ACDPs) (Nortek, 2021c, 2021a; Park & Hwang, 2021) and Acoustic Doppler Velocimeters (Nortek, 2021b; Teledyne RD Instruments, 2009b; Cisewski et al., 2010; Teledyne RD Instruments, 2009a; Cisewski et al., 2021) are all still suitable for observing upwelling and downwelling currents from migrating aggregates of zooplankton even up to $5D$ downstream of the aggregation. As can be seen in figure S6, the Gaussian decay of the velocity signature still confines the usefulness of velocimetry techniques to the immediate vicinity of the jet. However, because of the gradual expansion of the jet downstream of the aggregation, the horizontal distance from

the axis of the migration where the velocity signature can be detected gradually increases downstream of the migration.

By comparison, the limited vertical extent of the jet in this model has somewhat reduced the overall magnitude of the magnetic signature distribution and choice of normalization using the aggregation size versus jet width. Furthermore, the power-law decay of the signature is slightly faster than the y^{-1} predicted by the previous models. This feature is evidenced by the dashed gray line showing the nominal results from the previous section for comparison. However, at fixed horizontal distances, there is a relative enhancement of the magnetic signature with downstream distance from the migration outside the velocity jet due to the entrainment and jet spreading. While the detection distances for state-of-the-art fluxgate magnetometers (Bartington Instruments, 2022; Magson GmbH, 2022; Metrolab Technology SA, 2022) and Nitrogen-vacancy (NV) centers (Wolf et al., 2015) are significantly reduced compared to the previous models, each detection distance still extends approximately an order of magnitude further than the velocimetry techniques according to this model.

Table S1. Summary of Common Marine Velocimetry Techniques

Table S2. Summary of Various Magnetometry Techniques

References

Bartington Instruments. (2022). *Mag-13 ® Three-Axis Magnetic Field Sensors.*

Bastankhah, M., & Porté-Agel, F. (2014, oct). A new analytical model for wind-turbine wakes. *Renewable Energy*, *70*, 116–123. doi: 10.1016/J.RENENE.2014.01.002

Bastankhah, M., & Porté-Agel, F. (2016, nov). Experimental and theoretical study of

wind turbine wakes in yawed conditions. *Journal of Fluid Mechanics*, *806*, 506–541. Retrieved from https://www.cambridge.org/core/journals/journal-of-fluid-mechanics/article/experimental-and-theoretical-study-of-wind-turbine-wakes-in-yawed-conditions/400859134E38F340C8811FD7AAD0CE05 doi: 10.1017/JFM.2016.595

Bertuccioli, L., Roth, G. I., Katz, J., & Osborn, T. R. (1999). A submersible particle image velocimetry system for turbulence measurements in the bottom boundary layer. *Journal of Atmospheric and Oceanic Technology*, *16*(11), 1635–1646. doi: 10.1175/1520-0426(1999)016$\langle$1635:aspivs$\rangle$2.0.co;2

Chen, K., Deng, M., Wu, Z., Luo, X., & Zhou, L. (2020, may). A compact ocean bottom electromagnetic receiver and seismometer. *Geoscientific Instrumentation, Methods and Data Systems*, *9*(1), 213–222. doi: 10.5194/GI-9-213-2020

Chulliat, A., Brown, W., Alken, P., Beggan, C., Nair, M., Cox, G., ... Paniccia, M. (2020). *The US/UK World Magnetic Model for 2020-2025* (Tech. Rep.). doi: 10.25923/ytk1-yx35

Cisewski, B., Hátún, H., Kristiansen, I., Hansen, B., Larsen, K. M. H., Eliasen, S. K., & Jacobsen, J. A. (2021, jan). Vertical Migration of Pelagic and Mesopelagic Scatterers From ADCP Backscatter Data in the Southern Norwegian Sea. *Frontiers in Marine Science*, *7*, 1176. Retrieved from https://www.frontiersin.org/articles/10.3389/fmars.2020.542386/full doi: 10.3389/fmars.2020.542386

Cisewski, B., Strass, V. H., Rhein, M., & Krägefsky, S. (2010, jan). Seasonal variation of diel vertical migration of zooplankton from ADCP backscatter time series data

in the Lazarev Sea, Antarctica. *Deep Sea Research Part I: Oceanographic Research Papers*, *57*(1), 78–94. Retrieved from www.elsevier.com/locate/dsrihttps://linkinghub.elsevier.com/retrieve/pii/S0967063709001976 doi: 10.1016/j.dsr.2009.10.005

Dabiri, J. O. (2010, jun). Role of vertical migration in biogenic ocean mixing. *Geophysical Research Letters*, *37*(11), L11602. doi: 10.1029/2010GL043556

Dewar, W. K., Bingham, R. J., Iverson, R. L., Nowacek, D. P., St. Laurent, L. C., & Wiebe, P. H. (2006, jul). Does the marine biosphere mix the ocean? *Journal of Marine Research*, *64*(4), 541–561. doi: 10.1357/002224006778715720

Houghton, I. A. (2019). *Physical and biogeochemical impacts of migrating zooplankton aggregations* (Doctoral dissertation, Stanford University). Retrieved from http://purl.stanford.edu/qf211fm0762

Houghton, I. A., Koseff, J. R., Monismith, S. G., & Dabiri, J. O. (2018). Vertically migrating swimmers generate aggregation-scale eddies in a stratified column. *Nature*. Retrieved from https://doi.org/10.1038/s41586-018-0044-z doi: 10.1038/s41586-018-0044-z

Jensen, N. O. (1983). *A note on wind generator interaction* (Tech. Rep.). Risø National Laboratory.

Jin, T. (2019). *Underwater particle image velocimetry (piv) measurement of turbulence over mussel bed in a deepsite of lake michigan* (Unpublished doctoral dissertation). The University of Wisconsin-Milwaukee.

Katija, K., & Dabiri, J. O. (2008, apr). In situ field measurements of aquatic animal-fluid

interactions using a Self-Contained Underwater Velocimetry Apparatus (SCUVA). *Limnology and Oceanography: Methods*, *6*(4), 162–171. doi: 10.4319/lom.2008.6.162

Magson GmbH. (2022). *Digital Fluxgate Magnetometer.* Retrieved from www.magson.de

Metrolab Technology SA. (2022). *THM1176 and TFM1186 Key Specifications.* Retrieved 2022-05-09, from https://www.metrolab.com/wp-content/uploads/2020/11/THM1176-TFM1186-Key-specifications.pdf

Munk, W. H. (1966). Abyssal recipes. *Deep Sea Research and Oceanographic Abstracts*, *13*, 707–730.

Nortek. (2021a). *Aquadopp 6000 m.* Retrieved 2022-03-16, from https://www.nortekgroup.com/products/aquadopp-6000-m/pdf

Nortek. (2021b). *Signature1000 Current Profiler.* Retrieved 2022-03-16, from https://www.nortekgroup.com/products/signature-1000/pdf

Nortek. (2021c). *Vector - 300m Velocimeter.* Retrieved 2022-03-15, from https://www.nortekgroup.com/products/vector-300-m/pdf

Omand, M. M., Steinberg, D. K., & Stamieszkin, K. (2021, aug). Cloud shadows drive vertical migrations of deep-dwelling marine life. *Proceedings of the National Academy of Sciences*, *118*(32). Retrieved from https://pnas.org/doi/full/10.1073/pnas.2022977118 doi: 10.1073/pnas.2022977118

Park, H., & Hwang, J. H. (2021, aug). A Standard Criterion for Measuring Turbulence Quantities Using the Four-Receiver Acoustic Doppler Velocimetry. *Frontiers in Marine Science*, *8*, 1128. Retrieved from https://www.frontiersin.org/articles/10.3389/fmars.2021.681265/full doi: 10.3389/fmars.2021.681265

Rankine, W. (1865). On the Mechanical Principles of the Action of Propellers. *Transaction of the Institute of Naval Architects*, *6*, 13–39.

Shapiro, C. R., Gayme, D. F., & Meneveau, C. (2018). Modelling yawed wind turbine wakes: A lifting line approach. *Journal of Fluid Mechanics*, *841*, R11–R112. doi: 10.1017/jfm.2018.75

Teledyne RD Instruments. (2009a). *Ocean Surveyor.* Retrieved 2022-05-10, from www.teledynemarine.com

Teledyne RD Instruments. (2009b). *Workhorse Long Ranger.* Retrieved 2022-05-10, from www.teledynemarine.com

Wang, B., Liao, Q., Bootsma, H. A., & Wang, P. F. (2012, jun). A dual-beam dual-camera method for a battery-powered underwater miniature PIV (UWMPIV) system. *Experiments in Fluids*, *52*(6), 1401–1414. Retrieved from https://link.springer.com/article/10.1007/s00348-012-1265-9 doi: 10.1007/S00348-012-1265-9

Wilhelmus, M. M., & Dabiri, J. O. (2014). Observations of large-scale fluid transport by laser-guided plankton aggregations. *Physics of Fluids*, *26*(10), 1–12. doi: 10.1063/1.4895655

Wolf, T., Neumann, P., Nakamura, K., Sumiya, H., Ohshima, T., Isoya, J., & Wrachtrup, J. (2015, oct). Subpicotesla diamond magnetometry. *Physical Review X*, *5*(4), 041001. Retrieved from https://journals.aps.org/prx/pdf/10.1103/PhysRevX.5.041001 doi: 10.1103/PhysRevX.5.041001

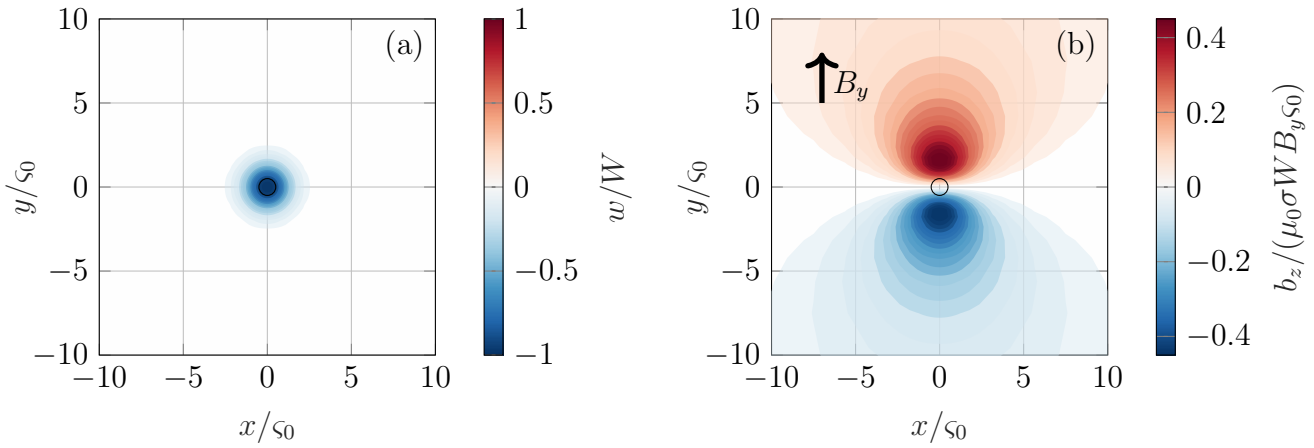

Figure S1. Plots of the dimensionless velocity and magnetic fields. (a) Contours of the vertical velocity component in the xy-plane. (b) Contours of the dimensionless vertical magnetic field component ($b_z/(\mu_0\sigma W B_y\varsigma_0)$) in the xy-plane. The lobed structure of the magnetic field follow a sinusoidal dependence with azimuthal angle. The peak values occur approximately $\sqrt{2}\varsigma_0$ away from the center of the migration. In each panel, the black circle indicates the region of radius, ς_0, centered on the aggregation location. The Gaussian velocity distribution in (a) decays significantly faster with distance from the migration than the corresponding magnetic signature (b).

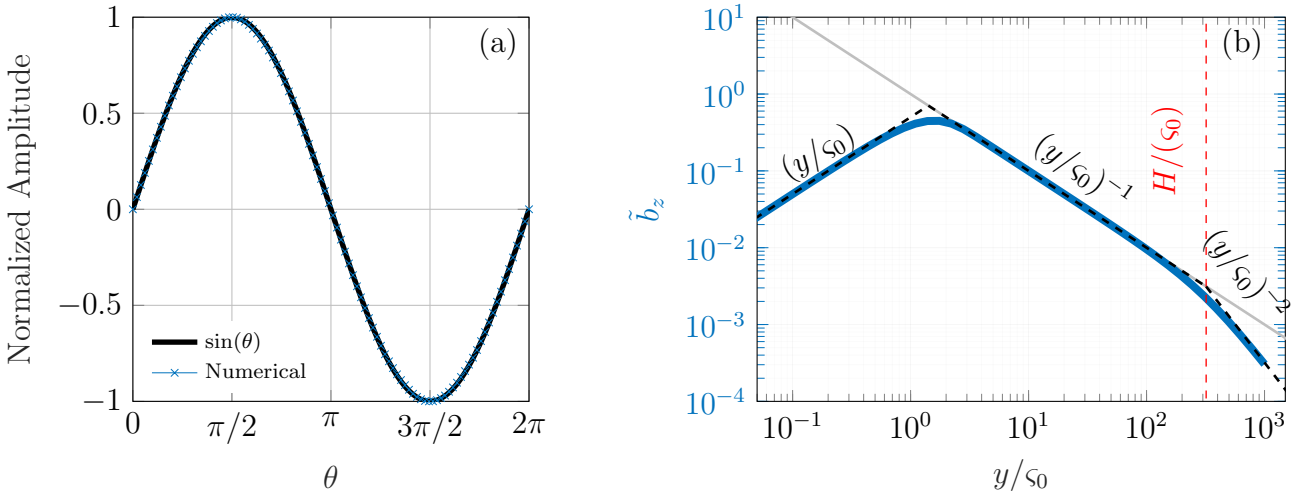

Figure S2. Comparison of numerical results with Rankine magnetic field model. (a) Normalized magnetic field amplitude as a function of azimuthal position in the xy-plane relative around the center of the migration. The azimuthal angle is taken with respect to the positive x axis. The amplitude variation exhibited by the magnetic field (blue x symbols) is computed for location at a distance ς_0 from the aggregation center and found to agree well with the sinusoidal approximation (solid black line). (b) Decay of magnetic signature with distance along the y-axis (North-South direction). Blue lines show the vertical magnetic field signature computed numerically along the y-axis. Dashed black lines show the Rankine model results along the y-axis. Three distinct regimes are observed 1) a y/ς_0 growth in the migration, 2) a ς_0/y decay for $y/\varsigma_0 > \sqrt{2}$, and , 3) a $(\varsigma_0/y)^2$ decay for $y/\varsigma_0 > H/\varsigma_0$. Gray line shows the solution for the Dirac Delta velocity model. Here, $H = 320\varsigma_0$.

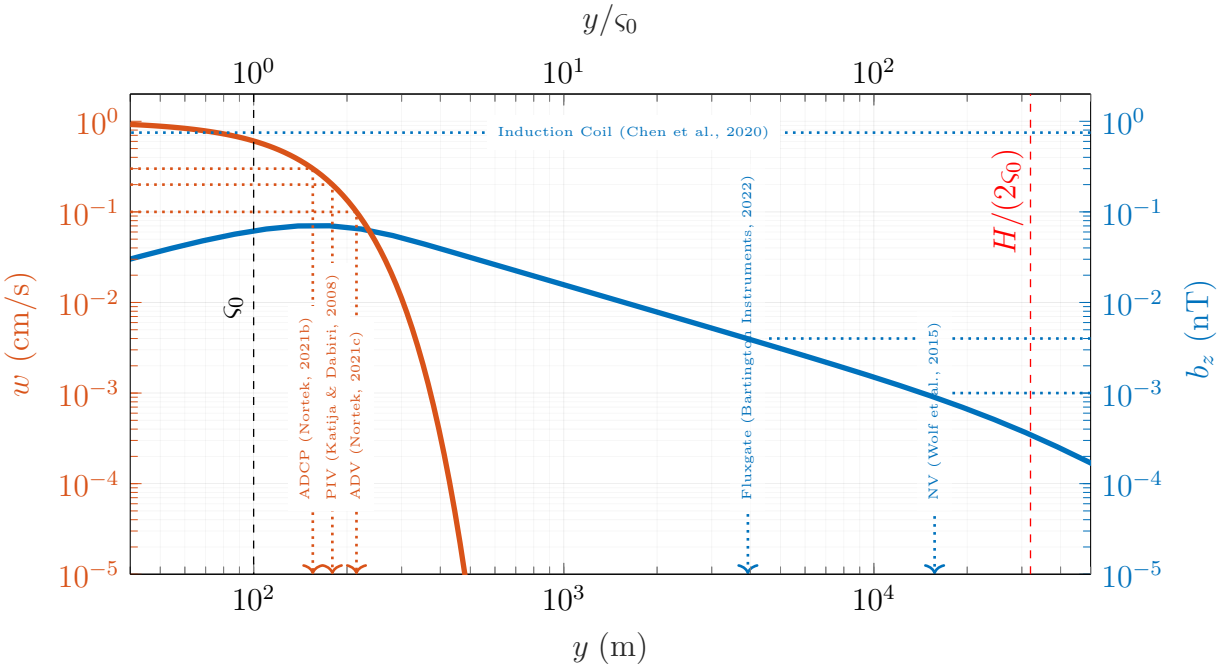

Figure S3. Profile of the dimensional magnetic field strength compared with the velocity signature along the y-axis. Solid blue lines show the magnetic field signature along the y-axis ($x = 0$). Solid orange lines show the velocity field signature along the y-axis ($x = 0$). Here we choose representative values of $B_{geo} = 25\mu$T, $\varsigma_0 = 100$ m, $\sigma = 5$ S/m, $W = 1$ cm/s, giving a representative magnetic signature magnitude of 157 pT. Dashed lines in orange and blue indicate the relative sensitivity limits of different velocimetry and magnetometry techniques, respectively. Red dashed line represents the height of the resolved velocity wake.

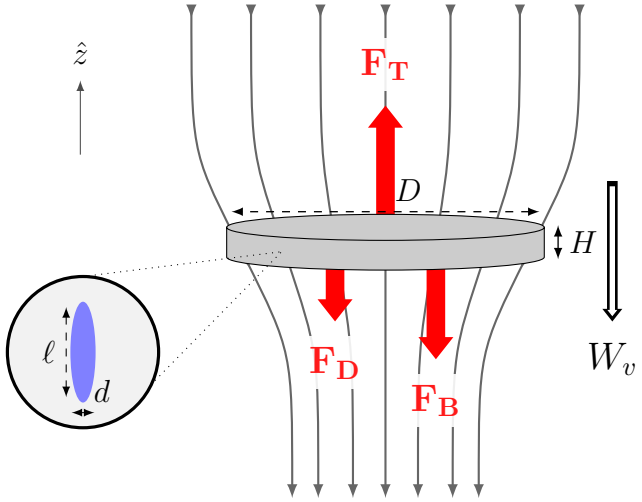

Figure S4. Diagram of the actuator disk model in its inertial frame. The aggregation is modeled as a porous disk of diameter, D, and height, H, shown in gray. The aggregation is assumed to climb upwards along the positive $\hat{z}$ direction at a constant velocity, W_v. The force balance of the actuator disk is shown where the upwardly directed thrust force (F_T) shown in blue is balanced by the downward directed buoyancy (F_B) and drag (F_D) forces shown in orange. The individual animals are modeled as prolate spheroids, indicated in light blue with body length, ℓ, and width, d.

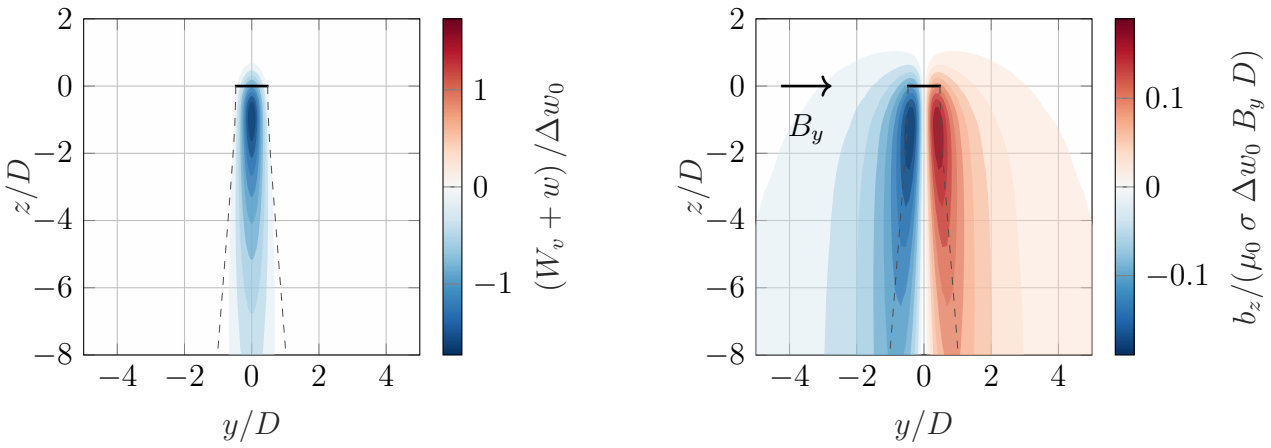

Figure S5. Plots of the dimensionless magnetic and velocity fields. In each panel, the solid black line represents the actuator disk of diameter, D, and the dashed line indicates the nominal width of the aggregation jet given by $\pm 2\varsigma_0 d_w(z)$ in equation 40. (a) Contour plot of the vertical jet velocity generated by the aggregation in the yz-plane. The velocity in the jet is largest immediately behind the aggregation and decays downstream with distance from the migration. (b) Contour plot of the dimensionless vertical magnetic field component ($b_z/(\mu_0 \sigma \Delta w_0 B_y D)$) in the yz-plane. Like the jet velocity, the magnetic signature extends downstream from the aggregation and decays quickly upstream of the migration. However, as in the previous models, the magnetic signature persists further from the aggregation location along the horizontal directions than the jet velocity signature.

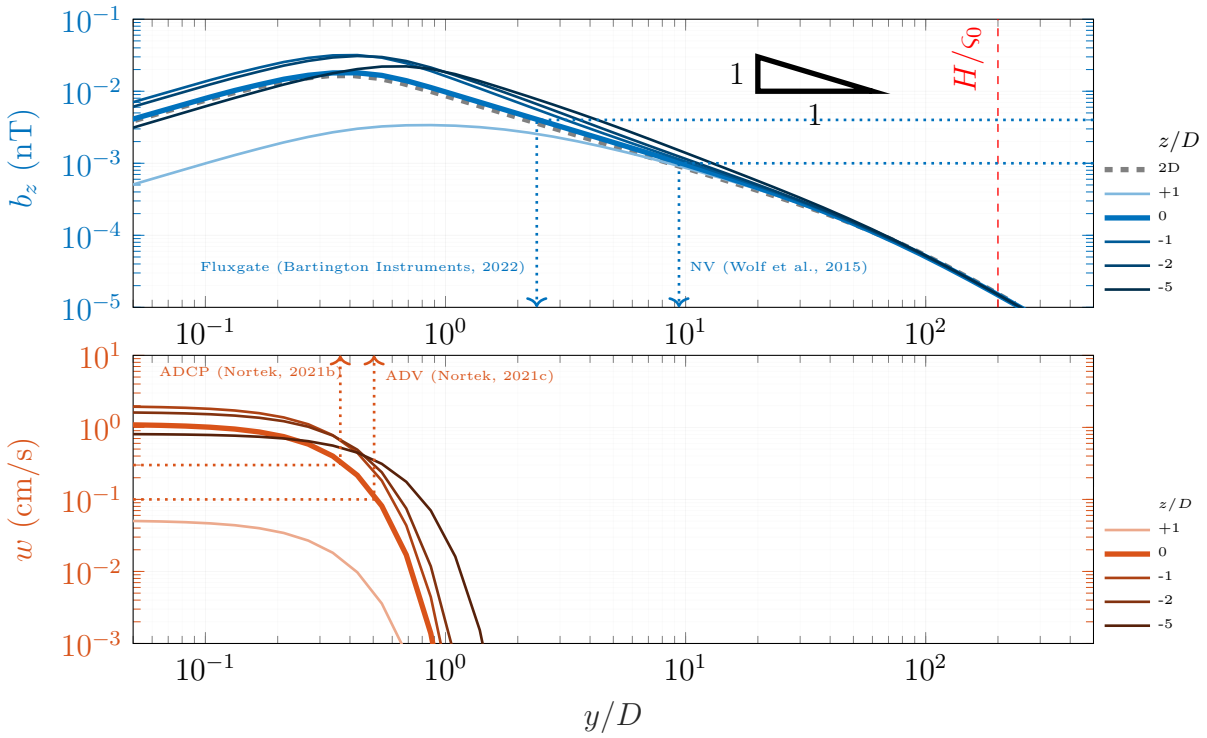

Figure S6. Profile of a representative dimensional (a) aggregation jet velocities and (b) corresponding vertical magnetic field strengths as a function of distance along the y-axis at different heights. Representative values of $B_{geo} = 25\mu$T, $D = 100$ m, $\sigma = 5$ S/m, $\Delta w_0 = 1$ cm/s, $k_w = 0.0834$ and $\varsigma_0 = 0.235D$ were chosen for the migration giving a representative magnetic signature magnitude of 157 pT. Solid orange and blue lines show the vertical jet velocity and vertical magnetic field component along the y-axis ($x = 0$) at vertical locations $z/D = -5, -2, -1, 0,$ and 1. Darker shades of each respective color indicate lower heights with the thick line denoting the height of the aggregation itself. Dotted lines indicate the typical resolution or sensitivity limit of corresponding velocimetry and magnetometry techniques. The dashed gray line in (b) indicates the nominally equivalent magnetic signature generated a 2D Gaussian jet of infinite extent (see equation 31). Red dashed line represents the height of the resolve velocity jet.

TABLE I. **Marine Velocimetry Techniques**

Technique	Velocity Accuracy $\mathrm{mm{\cdot}s^{-1}}$	Data Dimension	Velocity Components	Measurement Domain Size	References
Particle Image Velocimetry (PIV)	~ 1	Area (2D)	u,v	$0.200\,\mathrm{m} \times 0.200\,\mathrm{m}$	Bertuccioli *et al.* [18]
	~ 2	Area (2D)	u,v	$0.150\,\mathrm{m} \times 0.150\,\mathrm{m}$	Katija and Dabiri [10]
	~ 1	Area (2D)	u,v	$0.075\,\mathrm{m} \times 0.095\,\mathrm{m}$	Wang *et al.* [19]
	~ 1	Area (2D)	u,v	$0.100\,\mathrm{m} \times 0.200\,\mathrm{m}$	Jin [20]
				Cyl. - (dia. $\times$ ht.)	
Acoustic Doppler Velocimeter (ADV)	$1 \pm 0.5\%$	Point	u,v,w	$0.015\,\mathrm{m} \times 0.005 - 0.020\,\mathrm{m}$	Nortek Vector - 300 m [11]
	$5 \pm 1\%$	Point	u,v,w	$0.75\,\mathrm{m}$	Nortek Aquadopp - 6000 m [12]
	30	Point	u,v,w	$0.006\,\mathrm{m} \times\ 0.001 - 0.0091\,\mathrm{m}$	Park and Hwang [13]
				Range (Cell Size)	
Acoustic Doppler Current Profiler (ADCP)	$3 \pm 0.3\%$	Linear (1D)	u,v,w	$30\,\mathrm{m}\,(0.2 - 2\,\mathrm{m})$	Nortek Signature - 1000 m [9]
	$5 \pm 1\%$	Linear (1D)	u,v,w	$600\,\mathrm{m}\,(4 - 32\,\mathrm{m})$	Teledyne Workhorse Long Ranger [14] Cisewski *et al.* [15]
	$5 \pm 1\%$	Linear (1D)	u,v,w	$> 400\,\mathrm{m}\,(8\,\mathrm{m})$	Ocean Surveyor 150kHz [16] ,Cisewski *et al.* [17]
				Cyl. - (dia. $\times$ ht.)	
Laser Doppler Velocimeter (LDV)	——	Point	u,v	$0.0001\,\mathrm{m} \times 0.00015\,\mathrm{m}$	Trowbridge and Agrawal [31]
	2.7	Point	u,w	$0.0003\,\mathrm{m} \times 0.003\,\mathrm{m}$	Agrawal and Aubrey [32]
	~ 0.01	Point	u	$0.00022\,\mathrm{m} \times 0.0047\,\mathrm{m}$	Fowlis *et al.* [33]

TABLE II. **Magentometry Techniques**:

Technique	Measurement Type	Sensitivity ($nT/\sqrt{Hz}$)	Resolution (nT)	Nominal Instrument Size	Reference
Fluxgate Magnetometer	Vector	$< 4 \times 10^{-3}$ at 1 Hz	——	$3.0 \times 3.0 \times 25.0$ cm^3	Barington Instruments Mag-13 [6]
	Vector	$< 15 \times 10^{-3}$	7.75×10^{-3}	$5.0 - 7.0$ cm dia. $\times$ 4.0 cm	Magson GmbH MFG-2S[24]
	Vector	——	± 100	$7.0 \times 3.0 \times 3.2$ cm^3	Metrolab THM1186 [25]
	Vector	< 0.7	0.1	1.0 cm (dia.) $\times$ 4.0 cm (ht.)	Fluxmaster [34]
Superconducting Quantum Interference Device (SQUID)[a]	Vector	7×10^{-6} [b]	10×10^{-9}	——	Faley *et al.* [35]
Nitrogen-Vacancy Center	Vector	900×10^{-6}	100×10^{-6}	——	Wolf *et al.* [7]
	Vector	7	——	$7 \times 7 \times 11$ cm^3	Webb *et al.* [36]
	Vector	9	57.6	~ 1.5 cm (dia.) $\times$ 3 cm (ht.)	Kuwahata *et al.* [37]
Inductive Pickup Coil [c]	Vector	100×10^{-6}at 1 Hz	2×10^{-6}	~ 5 cm dia. $\times$ 110 cm	Chen *et al.* [8]
	Vector	75×10^{-3}at 0.01 Hz	——	~ 7 cm dia. $\times$ 134 cm	KMS Technologies LEMI-152 [38]
Hall-Effect Sensor	Vector	——	$\pm 20 \times 10^3$	$7.6 \times 2.25 \times 1.4$ cm^3	Metrolab THM1176 [25]
Optically Pumped Magnetometer					
Potassium Vapor	Total Field	200×10^{-6}	100×10^{-6}	~ 5 cm dia. $\times$ 10 cm	GEM GSMP-35 [39]
Rubidium-87 Vapor	Total Field	14×10^{-6}	——	——	Lucivero *et al.* [40]
	Total Field	14×10^{-6}	——	——	Limes *et al.* [41]
SERF[d] Potassium Vapor	Vector	540×10^{-9}	——	~ 0.5 cm (dia.) $\times$ 2.1 cm (ht.)	Kominis *et al.* [42]
	Vector	160×10^{-9}	——	10 cm (dia.) $\times$ 10 cm (ht.)	Dang *et al.* [43]

[a] Requires cryogenic cooling
[b] at 77.4 K
[c] Not suitable for DC magnetic fields.
[d] Spin Exchange Relaxation-Free, Requires near zero magentic field conditions